ARTICLE NO. 79-0134R

J80-046

Calculation of Transonic Aileron Buzz

20001
20005
20009

J. L. Steger* and H. E. Bailey†
NASA Ames Research Center, Moffett Field, Calif.

An implicit finite-difference computer code that uses a two-layer algebraic eddy viscosity model and exact geometric specification of the airfoil has been used to simulate transonic aileron buzz. The calculated results, which were performed on the Illiac IV parallel computer processor and the Control Data 7600 computer, are in essential agreement with the original expository wind-tunnel data taken in the Ames 16-ft wind tunnel just after World War II. These results and a description of the pertinent numerical techniques are included.

I. Introduction

In a previous publication,[1] a general viscous airfoil computer code that uses an implicit finite-difference scheme was described. By comparison to available numerical and experimental data, the computer code was shown to be accurate for various inviscid and viscous, steady and unsteady transonic flows about airfoils. The computer program employs general coordinate transformations that allow arbitrary body shape and motion.

The purpose of this paper is twofold: 1) to further demonstrate the numerical technique and 2) to further investigate unsteady flow phenomena about airfoils. To these ends, the calculation of aileron buzz phenomena was undertaken using the Control Data Corporation 7600 computer and the Illiac IV parallel processor computer. The latter machine is more economical for extensive viscous flowfield calculations than the Control Data machine.

The problem of transonic aileron buzz was apparently first encountered by pilots in World War II. Because later flight tests of the P-80 (i.e., F-80) proved hazardous,[2] Erickson and Stephenson[3] undertook wind tunnel tests of a P-80 half-span wing mounted in the Ames 16-ft wind tunnel. From these experiments, Erickson and Stephenson concluded that aileron buzz is a one-degree-of-freedom flutter in which shock-wave motion causes a phase shift in the response of the hinge moment to the aileron movement. Oscillatory aileron motion was observed for various combinations of Mach number, geometry, and mechanical damping.

Although aileron buzz is no longer as serious a problem because of the introduction of hydraulically actuated controls, we can now use modern numerical techniques to explore questions still unanswered by experiment and simplified theory.[4] In this paper then, we begin to investigate the aileron buzz problem using numerical techniques. In Sec. II, the governing flowfield equations are briefly sketched. The numerical method, with extensions over Ref. 1, and the boundary and grid treatment of the moving aileron are reviewed in Sec. III. Finally, numerical results are discussed in Sec. IV and compared to the data of Ref. 3.

Presented as Paper 79-0134 at the AIAA 17th Aerospace Sciences Meeting, New Orleans, La., Jan. 15-17, 1979; submitted March 16, 1979; revision received Aug. 13, 1979.

Index categories: Aeroacoustics; Nonsteady Aerodynamics; Computational Methods.

*Research Scientist; presently with Flow Simulations, Inc., Sunnyvale, Calif. Member AIAA.

†Research Scientist.

II. Governing Equations

Flowfield Variables

As governing equations, we take the nondimensional thin-layer[1,5] Navier-Stokes equations subject to general transformation but kept in strong conservation-law form[6]

$$\partial_\tau \hat{q} + \partial_\xi \hat{f}501u\hat{F} = R_e^{-1}\partial_\eta \hat{S} \tag{1}$$

where $\xi = \xi(x,y,t)$, $\eta = \eta(x,y,t)$, and $\tau = t$, and the flux terms are defined as

$$\hat{q} = J^{-1}\begin{bmatrix}\rho\\ \rho u\\ \rho v\\ e\end{bmatrix}, \qquad \hat{E} = J^{-1}\begin{bmatrix}\rho U\\ \rho uU + \xi_x p\\ \rho vU + \xi_y p\\ (e+p)U - \xi_t p\end{bmatrix}$$

$$\hat{F} = J^{-1}\begin{bmatrix}\rho V\\ \rho uV + \eta_x p\\ \rho vV + \eta_y p\\ (e+p)V - \eta_t p\end{bmatrix}$$

$$\hat{S} = J^{-1}\begin{bmatrix}0\\ m_1 u_\eta + m_2 \eta_x\\ m_1 v_\eta + m_2 \eta_y\\ \mu^{-1}\kappa P_r^{-1}(\gamma-1)^{-1} m_1 \partial_\eta a^2 + m_1 (u^2+v^2)_\eta/2 + m_2(\eta_x u + \eta_y v)\end{bmatrix}$$

$$m_1 = \mu(\eta_x^2 + \eta_y^2), \quad m_2 = (\mu/3)(\eta_x u_\eta + \eta_y v_\eta)$$

$$J = \xi_x\eta_y - \xi_y\eta_x = (x_\xi y_\eta - x_\eta y_\xi)^{-1}$$

Here the variables have been nondimensionalized using ρ_∞, a_∞, and chord c as reference density, speed, and length. Throughout, ρ is density, p is pressure, u and v are Cartesian velocity components, and a is the sound speed. The total energy per unit volume e is defined by

$$e = (\gamma-1)^{-1}p + 0.5\rho(u^2+v^2) \tag{2}$$

while the contravariant velocities are defined as

$$U = \xi_t + \xi_x u + \xi_y v \tag{3a}$$

$$V = \eta_t + \eta_x u + \eta_y v \tag{3b}$$

The metrics ξ_t, ξ_x, etc. are determined once a mapping is defined. Usually, a numerical mapping is employed. The metrics are related to x_τ, x_ξ, etc. by the relations

$$\xi_x = Jy_\eta,\ \xi_y = -Jx_\eta,\ \xi_t = -x_\tau\xi_x - y_\tau\xi_y$$
$$\eta_x = -Jy_\xi,\ \eta_y = Jx_\xi,\ \eta_t = -x_\tau\eta_x - y_\tau\eta_y \tag{4}$$

Here ξ varies around the body surface while η varies away from the body surface, as indicated in Fig. 1. Throughout, the symbol $\hat{\ }$ denotes that the scalar or vector quantity is divided through by the Jacobian J.

We require that the body be mapped onto an η = constant plane. Consequently, the tangency condition is given by $V=0$. The no-slip condition requires that $U=0$ as well. For inviscid flow, a Kutta condition is satisfied by requiring that $U=0$ at the noncusped trailing edge of the airfoil. Note that the equations and boundary conditions are valid for steady or unsteady body motion, including deforming body shapes.

Further details of the equations are given in Ref. 1, although in Ref. 1 we failed to emphasize that Eq. (1) is kept in strong conservation-law form for two reasons. First, the differential (and difference) equations in strong conservation-law form can, in principle, capture correct weak solutions as the mesh is refined. Second, we prefer to avoid source terms due to coordinate transformations. Such source terms usually have associated eigenvalues with positive and negative real parts. If the source terms are then sufficiently dominant, they would tend to make the finite-difference, time-marching process less stable or even weakly unstable.

For practical viscous flow calculations, a turbulence model is needed. The Cebeci algebraic two-layer eddy viscosity model as modified by Baldwin and Lomax[5] is used. The thin-layer approximation requires that $Re \gg 1$ and the previously noted constraint that the body be mapped onto an η = constant plane.

Aileron Motion

For a rigid aileron in two-dimensional flow, the motion of the aileron is governed by the one-degree-of-freedom equation:

$$I_a\ddot{\delta}_a + k\delta_a = H(t) \tag{5}$$

where I_a is the aileron mass moment of inertia about the hinge line, k is a spring constant, and H is the aerodynamic forcing term. In our simulations, we take $k=0$ (the flap is not constrained other than by the hinge point), and H is simply the aerodynamic moment about the hinge line. Here δ_a is taken to be positive for a downward deflection of the aileron (i.e., flap at positive angle of attack) as sketched in Fig. 1. Throughout, the moment and moment coefficient about the hinge point x_H are defined as

$$H = \int (p-p_\infty)(x-x_H)\,c\,dx;\quad x_H \le x \le x_{te}$$
$$C_H = H/(\tfrac{1}{2}\rho_\infty(u_\infty^2+v_\infty^2)(x_{te}-x_H)c^2) \tag{6}$$

where c is the chord and as a flap reference area we use $(x_{te}-x_H)c$. The moment is positive in the clockwise direction, and the sign of Eq. (6) must be changed for the flap lower surface.

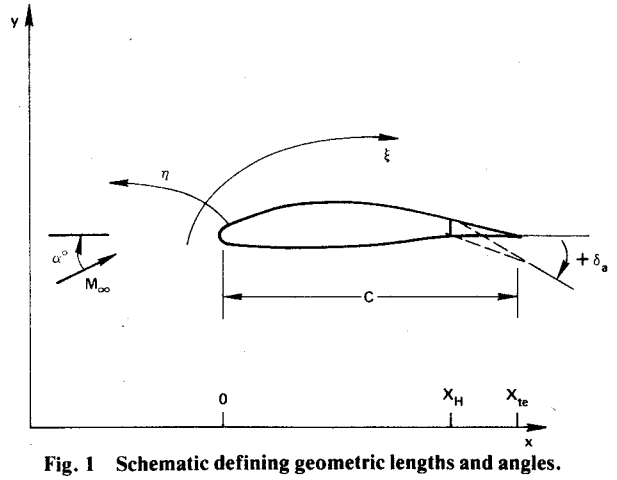

Fig. 1 Schematic defining geometric lengths and angles.

III. Numerical Method

To numerically simulate aileron buzz, Eqs. (1) and (5) are discretized in space and time and are solved simultaneously as follows. From initial or previous time-level data, the moment H about the hinge line is computed and used to predict a value of δ_a at the new time level. The flap is deflected to the new value of δ_a and new grid point locations are found, as will be described. New metrics ξ_t, ξ_x, etc. are then computed at each grid point and used in an implicit finite-difference algorithm for Eq. (1) to advance the flow variables to the next time step. This process is repeated for each subsequent time step. Details of the numerical procedure are presented in this section. Note that while Eqs. (1) and (5) are solved simultaneously at each time step, Eq. (5) is treated explicitly and Eq. (1) is solved implicitly.

Airfoil Finite-Difference Procedure

The thin-layer flowfield equations are solved using an implicit finite-difference algorithm. Although the algorithm has been previously detailed[1,7,8] it is briefly reviewed below for completeness. Additional options in the numerical procedure are also sketched.

The difference equations in approximate factorized implicit delta form are given by

$$\begin{aligned}&(I+h\delta_\xi\hat{A}^n - J^{-1}\epsilon_i h\nabla_\xi\Delta_\xi J)(I+h\delta_\eta\hat{B}^n\\ &\quad - J^{-1}\epsilon_i h\nabla_\eta\Delta_\eta J - R_e^{-1}h\delta_\eta J^{-1}\hat{M}^n)(\hat{q}^{n+1}-\hat{q}^n)\\ &\quad = -h(\delta_\xi\hat{E}^n + \delta_\eta\hat{F}^n - R_e^{-1}\delta_\eta\hat{S}^n) + \beta(\hat{q}^n-\hat{q}^{n-1})\\ &\quad - \epsilon_e h J^{-1}[(\nabla_\xi\Delta_\xi)^2 + (\nabla_\eta\Delta_\eta)^2]J\hat{q}^n\end{aligned} \tag{7}$$

where $\beta=0$ for Euler implicit differencing or $\frac{1}{3}$ for three-point backward implicit time differencing. Here $h=(1-\beta)\Delta t$, n denotes the nth time level, and spatial indices have been deleted for clarity. As previously noted, the symbol $\hat{\ }$ implies division by J, e.g., $\hat{q}=(q/J)$. The matrices $\hat{A}$, $\hat{B}$, and $\hat{M}$ are the 4×4 Jacobian matrices, e.g., $\hat{A}=[\partial\hat{E}/\partial\hat{q}]$, and are detailed in Ref. 1. Unless ϵ_e and $\epsilon_i=0$, artificial dissipation terms are included in the difference approximation. Typically, ϵ_e is 0(1) and $\epsilon_i=2.5\epsilon_e$ (see Ref. 9 for more details), but both ϵ_e and ϵ_i may be much larger during an impulsive start from uniform initial data. The explicit smoothing term is of order four in the spatial step size, while the implicit term is of second order in the spatial step size times Δt. Values of ϵ_e and ϵ_i that vary in space have also been used with success, but optimum choices have not been completely investigated.

The operators ∇_ξ, Δ_η, etc. retain their conventional definitions, for example,

$$\Delta_\eta q_{j,k} = (q_{j,k+1} - q_{j,k})/\Delta\eta \tag{8}$$

and ∇ indicates a backward difference. However, δ_ξ and δ_η are symbolic difference operators that can assume various forms.[1] Here the δ_ξ and δ_η convection operators are three-point central-difference operators [cf. Eq. (A3)]. The viscous terms are central-differenced. Any one term has the form $\partial_\eta g\partial_\eta f$ and is differenced as

$$\begin{aligned}\delta_\eta g\delta_\eta f = [&(g_{j,k+1}+g_{j,k})(f_{j,k+1}-f_{j,k})\\ &-(g_{j,k}+g_{j,k-1})(f_{j,k}-f_{j,k-1})]/[2(\Delta\eta)^2]\end{aligned} \tag{9}$$

A simple way to achieve higher-order spatial accuracy for the convection terms is described in the Appendix.

Boundary conditions are imposed at the end of each time step in an explicit manner.[1] Pressure is updated along the body surface from the normal momentum relation and density is found from extrapolation in inviscid flow or from the adiabatic wall relation in viscous flow. In inviscid flow U is also found by extrapolation.

The explicit boundary condition treatment used here does not appear to cause any numerical stability limitation, but the boundary condition treatment is first order in time. To obtain second-order time accuracy at the boundaries, an implicit correction process has been easily implemented (only in the CDC 7600 computer code) by assuming that the time variation on the surface is the same as the time variation adjacent to the body surface, for example, for density

$$(\rho^{n+1}-\rho^n)_{j,k=1}=(\rho^{n+1}-\rho^n)_{j,k=2}+0(\Delta\eta\Delta t) \tag{10}$$

where $k=1$ corresponds to $\eta=0$. The remaining variables, ρu, ρv, and e, are corrected in a similar manner, although in viscous flow, adjustments should be made if $u=v=0$. The boundary relation, Eq. (10), is incorporated into the left-hand side of Eq. (7) because it is easily implemented in the delta form algorithm by adding two 4×4 diagonal matrices to the end of the block tridiagonal matrix in η. The relation, Eq. (10), is a correction for data near the boundary; after the entire field is updated from Eqs. (7) and (10), surface boundary data are re-evaluated solely from the previously described explicit relations.

The "C-type" grids shown in Figs. 2 and 3 have been used with the airfoil computer code. The grid shown in Fig. 2, used with the Control Data 7600 computer program, is generated by solving elliptic partial-differential equations as outlined in Refs. 10 and 11. The algebraically generated grid shown in Fig. 3 is used with the Illiac IV computer code. In either case, a smooth exponential grid stretching is used in η, while grid points in ξ are typically distributed, as indicated in Fig. 3.

Aileron and Grid Motion

The equation that governs the aileron angle of attack, Eq. (5), is differenced to second-order accuracy in time as

$$\delta_a^{n+1}-2\delta_a^n+\delta_a^{n-1}=(\Delta t)^2(H^n/I_a) \tag{11}$$

The value of δ_a^{n+1} is found from the explicit relation, Eq. (11), at the start of each time step using the known hinge moment at level n.

Once the aileron is deflected, a new grid has to be formed. On the Control Data machine, simple shearing transformations are used to avoid solving the grid generation equations at each time step. On the Illiac IV, which entails more complex programming techniques, we restrict the grid to a simple type that allows analytic introduction of the flap motion. Initially, we discuss grid deformation by the shearing transform.

A trailing edge portion of an airfoil with a simple sheared Cartesian grid is sketched in Fig. 4. As the flap moves down we can attempt to simply rotate each grid point with it. Grid point P in the figure, which has ordinates x, y, is moved to P' with new ordinates x', y' and aileron angle δ_a' by the relation

$$\left.\begin{aligned}x'&=x-(x_0-x_H)(\cos\delta_a-\cos\delta_a')g_1\\ y'&=y-(x_0-x_H)(\sin\delta_a-\sin\delta_a')g_2\end{aligned}\right\}x>x_H \tag{12}$$

where $x_0=(x-x_H)\sec\delta_a+x_H$ and $g_1=g_2=1$ for pure rotational movement of the grid points. This transformation is general and is easily imposed; however, unless g_1 and g_2 are properly modified, grid lines will usually cross and invalidate the one-to-one mapping (i.e., $J\to0$).

For transonic buzz calculations we chose to simply adjust the grid at each time step by using Eq. (12) with $g_1=0$ and

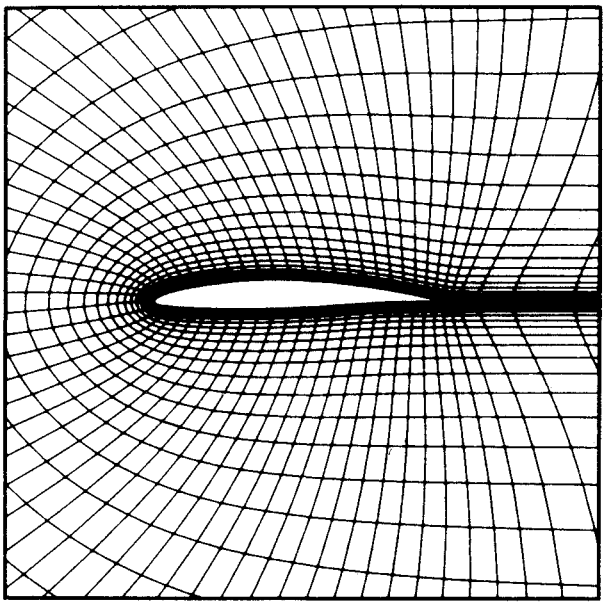

Fig. 2 Typical C-type grid detail near airfoil.

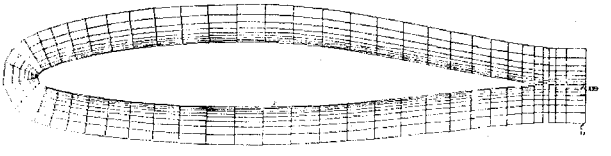

Fig. 3 Algebraic C-type grid about NACA 65-213 airfoil with sheared Cartesian-like mesh from near midchord to back boundary.

$g_2=1$; that is,

$$\begin{aligned}x'&=x\\ y'&=y-(x-x_H)(\sin\delta_a-\sin\delta_a')\end{aligned} \tag{13}$$

This is a simple shearing transform which can be used to adjust the curvilinear grids shown in Figs. 2 and 3. Its use insures that grid lines cannot cross as δ_a varies, and, as long as δ_a does not depart significantly from zero, use of Eq. (13) is quite satisfactory. The dashed lines in Fig. 4b illustrate its application to the sheared Cartesian-like grid. However, use of Eq. (13) does cause the airfoil to grow in length as the flap is deflected because the trailing edge point, for one, remains at the same x location as δ_a varies (see Fig. 4b). For a hinge point at $x_H/c=0.75$, a deflection of 20 deg causes the total airfoil to grow in length by 1.5% of chord.

In the Illiac IV version of the program, only grids such as that shown in Fig. 3 are used. The Cartesian-like rear grid and the simple form of Eq. (13) allow analytic evaluation of the matrices with aileron deflection; in particular,

$$\begin{aligned}&\xi_t=0\\ &\eta_t^{n+1}=-y_\tau\eta_y,\quad y_\tau=(x-x_H)\left(\frac{\tan\delta_a^n-\tan\delta_a^{n+1}}{\Delta t}\right)\\ &\xi_x=x^{-1},\quad \xi_y=0\\ &\eta_x^{n+1}=\eta_x^n-\eta_y(\tan\delta_a^n-\tan\delta_a^{n+1}),\quad \eta_y=(y_\eta)^{-1}\end{aligned} \tag{14}$$

IV. Results

In the experiments of Erickson and Stephenson,[3] the wing of a P-80 was mounted in the Ames 16-ft wind tunnel as shown in Fig. 5. The wing was supported at the tip to prevent bending and the aileron was allowed free motion about the

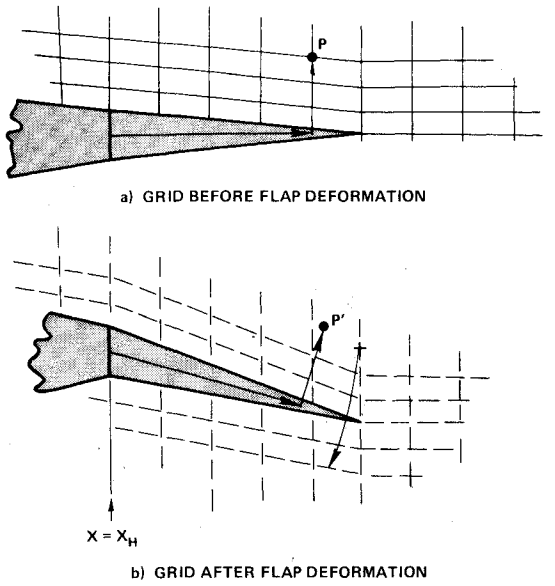

Fig. 4 Use of shearing transformation to avoid complicated regridding process with each increment of flap rotation.

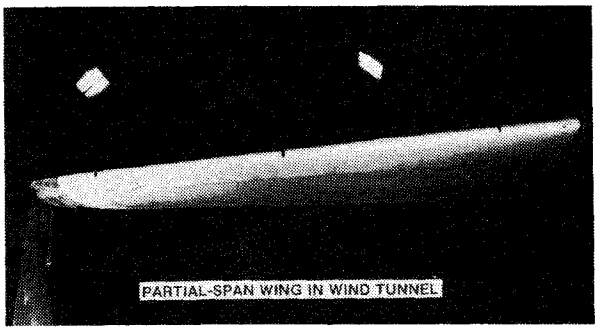

Fig. 5 Partial-span wing installed in wind tunnel.

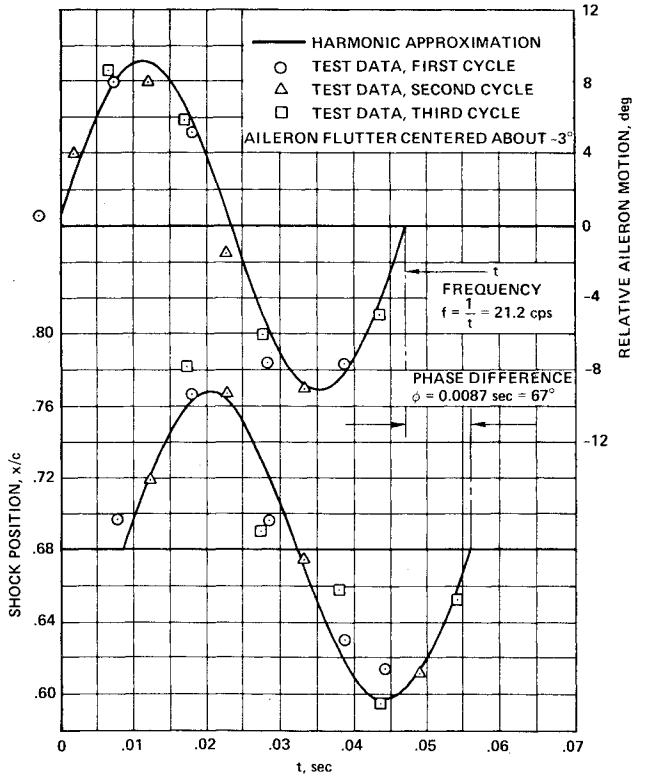

Fig. 6 Experimentally measured variation of aileron angle and normal shock position with time, $M_\infty = 0.82$, $\alpha = -1$ deg.

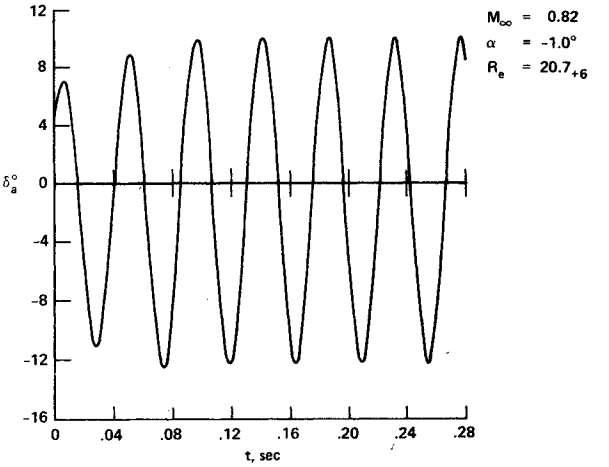

Fig. 7 Computed variation of aileron angle with time; aileron initially set to 4 deg.

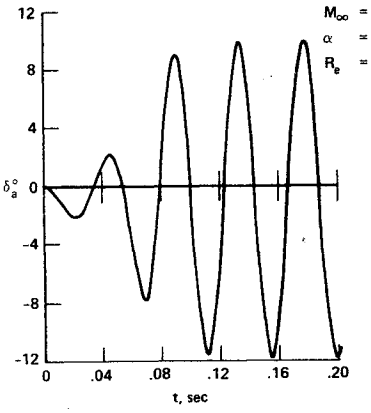

Fig. 8 Computed variation of aileron angle with time; aileron initially set at 0 deg.

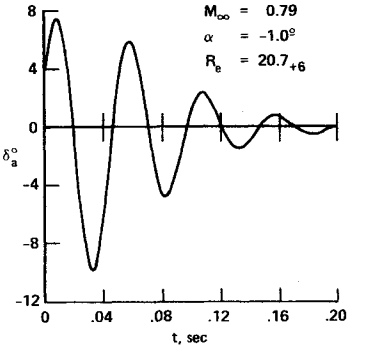

Fig. 9 Decay of aileron buzz with time.

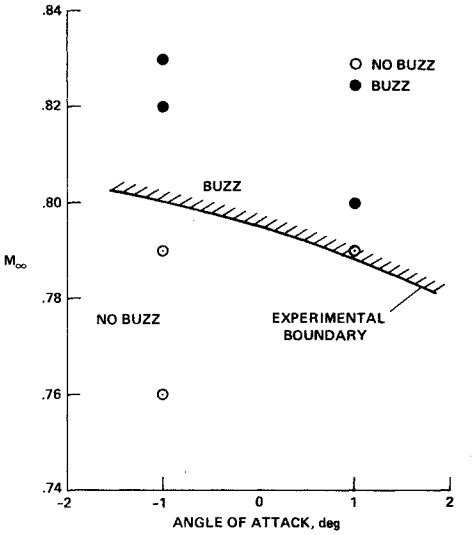

Fig. 10 Mach numbers and angles of attack over which buzz occurs.

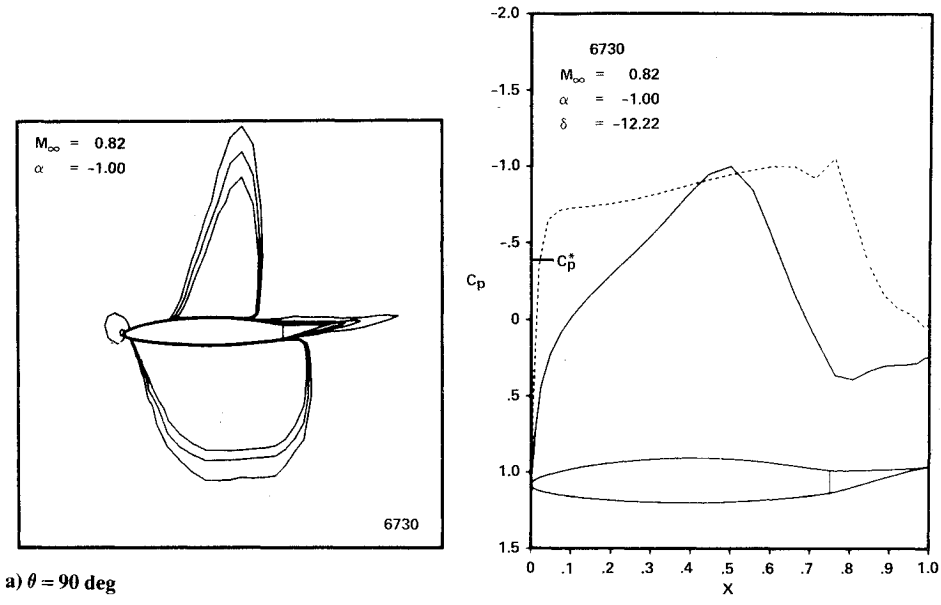

a) $\theta = 90$ deg

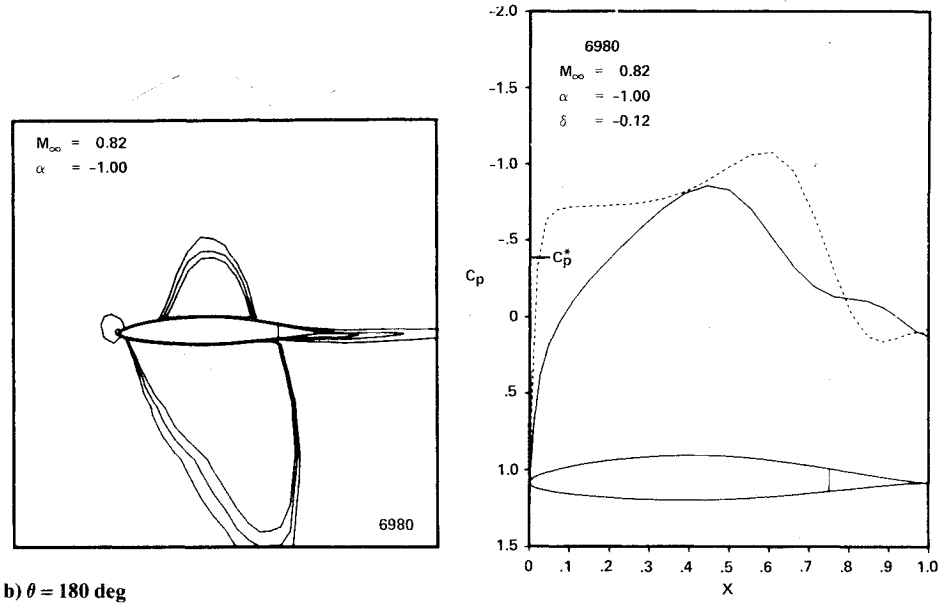

b) $\theta = 180$ deg

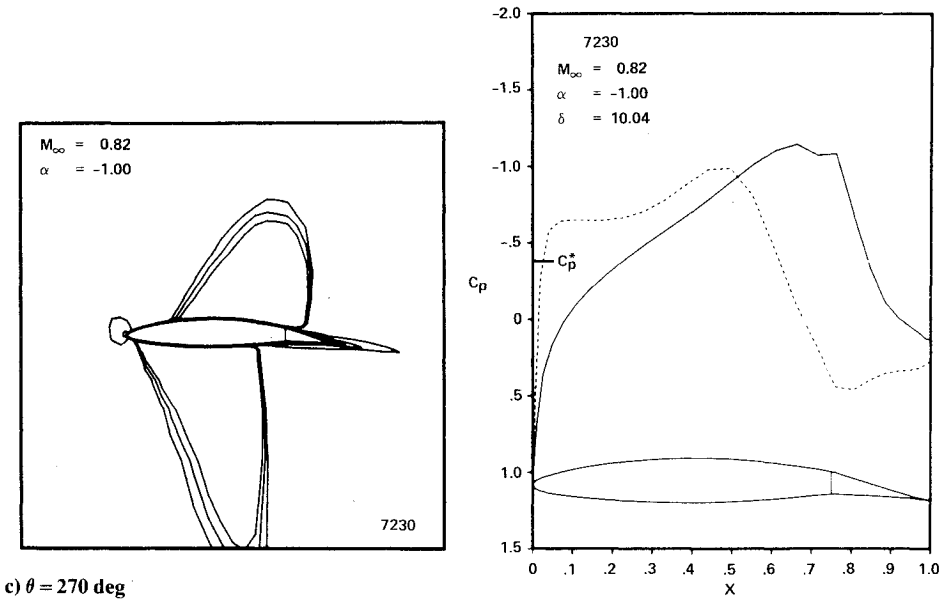

c) $\theta = 270$ deg

Fig. 11 Mach contour lines and C_p distributions during an aileron buzz cycle, $M_\infty = 0.82$, $\alpha = -1$ deg, $R_e = 20.7 \times 10^6$. Here $\theta = (t/t_p)^*$ 360 deg where t_p is the time to complete one cycle.

hinge line. In our two-dimensional calculation, the P-80 airfoil section, an NACA 65_1-213 $a=0.5$, was allowed free aileron motion about the hinge point at the 75% chord station. The Reynolds number was based on a mean chord length of 1.423 m (4.667 ft), and throughout we have taken ideal atmospheric sea-level values as the wind-tunnel stagnation conditions.

Numerical results were obtained using both the Control Data 7600 computer and the Illiac IV parallel processor. The scalar machine is easier to program and was used for initial code development as well as all inviscid flow calculations. The more time-consuming viscous flow simulations were carried out on the Illiac IV machine. For a spatial grid of 76×42 points, approximately 1½ s of Control Data 7600 computer time are needed to advance the solution one time step. A nondimensional time increment for viscous flow calculations is typically 0.005 to 0.01 where nondimensional time $\tilde{t}=ta_\infty/c$.

According to the experiment, at $M_\infty=0.82$ and $\alpha=-1$ deg, the aileron could be restrained at an angle near zero, and when freed, would buzz with amplitude and frequency as indicated in Fig. 6. In our numerical simulation the aileron would not buzz under these conditions. However, if the aileron was initially deflected to 4 deg, it would, on being released, buzz as indicated in Fig. 7. The computed frequency of 22.2 Hz (reduced frequency $\kappa=2\pi/(M_\infty\tilde{t}_p)=0.76$, where $\tilde{t}_p$ is the nondimensional time period) is in good agreement with the experimental value of 21.2 Hz. In the numerical calculation, the aileron deflects ±11.1 deg about the angle -1.1 deg, while the corresponding experimental values are ±9.2 deg about -3 deg.

In the numerical calculations at a slightly higher Mach number, $M_\infty=0.83$, the aileron does go into a buzz cycle when freed from a zero deflection position. An essentially steady-state solution was used as initial data. The buildup of aileron deflection angle as a function of time is indicated in Fig. 8. After four cycles, a quasi-steady-state is reached and the aileron oscillates at 22.7 Hz ($\kappa=0.765$).

At a lower Mach number, $M_\infty=0.79$, the aileron motion damps to a neutral value even though the flap was initially deflected 4 deg. Data from this calculation are displayed in Fig. 9.

Similar calculations to the preceding can be made at different airfoil angles of attack and a buzz boundary can thus be mapped. The beginnings of such a boundary curve determination are indicated in Fig. 10. Also shown is the experimentally found boundary which occurs at a somewhat lower Mach number. The flight-test-determined buzz boundary was encountered at a slightly lower Mach number than in the wind-tunnel data.[2]

Several frames from computer-generated film strips showing Mach contours and C_p distributions are shown in Figs. 11a-c at selected times for $\alpha=-1$ deg and $M_\infty=0.82$. Contour levels of $M=0.2$, 0.4, 0.6, 0.98, 1.0, and 1.02 were used in order to illustrate both the separated flow regions and sonic lines. The C_p distributions clearly demonstrate that the captured shock waves are being smeared over a significant portion of the airfoil. No attempt has yet been made to cluster additional points in the moving shock region.

From the C_p distributions it is possible to determine the shock position as a function of aileron deflection, and to compare these data to the experimental data shown in Fig. 6. Insofar as only the type of data shown in Fig. 11 were stored during the numerical calculation, the determination of the shock position is somewhat more subjective than we would like. Basing the shock location on the pressure gradient, we conclude that the upper-surface flow is shock free during part of the cycle, $\theta=180$-225 deg where $\theta=(t/t_p)*360$ deg. Consequently, we interpret our numerical results as shown in Fig. 12. As the flap deflects downward, a shock wave forms at its maximum downstream location and then, as the flap moves through a cycle, the shock moves upstream, weakens, and

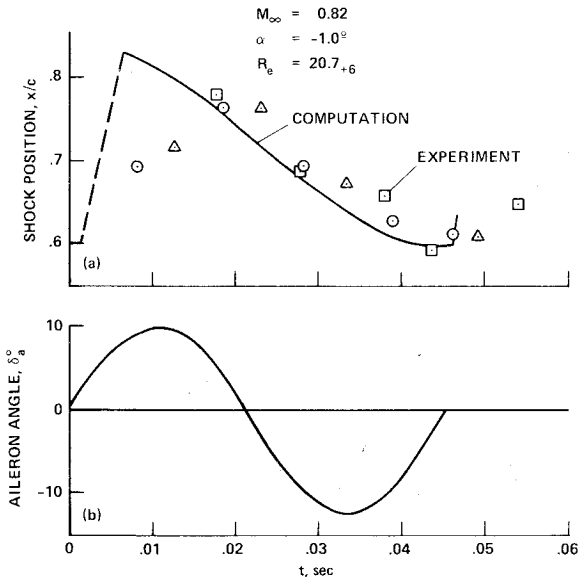

Fig. 12 Upper shock location vs time, $M_\infty=0.82$, $\alpha=-1$ deg.

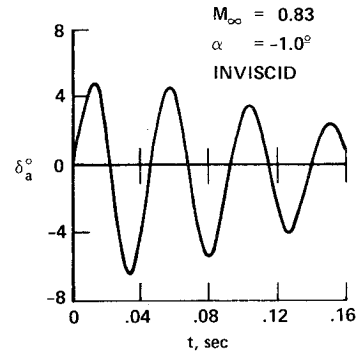

Fig. 13 Decay of aileron deflection with time in inviscid flow.

vanishes. (This type of shock-wave motion was observed experimentally by Tijdeman[12] and has been computed inviscidly by Ballhaus and Goorjian[13] and Magnus.[14] In both of these cases the flap motion was forced.) Figure 12 also contains the experimental shock locations as determined by Erickson and Stephenson from shadowgraphs. The extreme forward position of the shock is in good agreement, but the rearward excursions are not. Both sets of data show a phase difference between the shock motion and the aileron motion.

Representative inviscid flowfield results are shown in Figs. 13 and 14. These cases are initialized from steady-state flow with $\delta_a=0$ deg. The aileron motion was then forced to 4 deg, in a time-continuous way, and released. In inviscid flow at $M_\infty=0.83$ and $\alpha=-1$ deg, the aileron motion damps from a 4 deg perturbation (Fig. 13). As the aileron motion damps, the frequency decreases, but a typical value of frequency taken from Fig. 13 is 21.57 Hz ($\kappa=0.728$). In viscous flow, the aileron oscillates at this Mach number (see Fig. 8) as well as at the lower Mach number, $M_\infty=0.82$ (as shown in Fig. 7). At a higher Mach number, $M_\infty=0.84$, the aileron in inviscid flow goes into a divergent oscillatory growth (or the deflection angle exceeds ±45 deg). Here the frequency increases, but a typical value from Fig. 14 is 23.46 Hz ($\kappa=0.783$). Divergent aileron motion did not occur in a viscous flow calculation at $M_\infty=0.85$ (Fig. 15). From these data we find that while inviscid unsteady shock-wave motion is the driving force of transonic aileron buzz, the viscosity is nevertheless crucial and can both sustain and moderate the flap motion.

Finally, for the aileron held fixed at a higher Mach number, $M_\infty=0.85$, we find that the viscous flow does not reach a steady state but buffets at a frequency of about 26.6 Hz

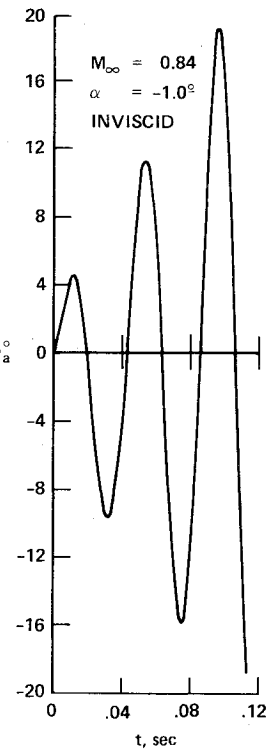

Fig. 15 Aileron buzz with predominant viscous effects.

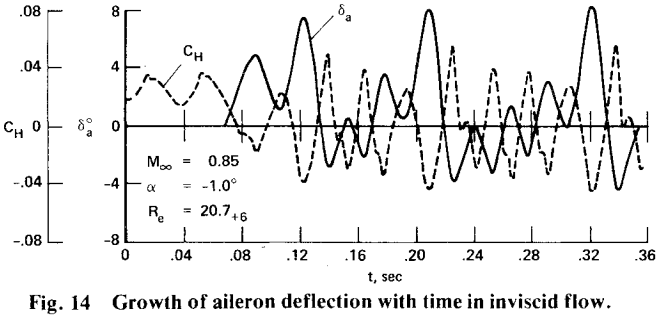

Fig. 14 Growth of aileron deflection with time in inviscid flow.

($\kappa = 0.86$). As shown in Fig. 15, if the aileron is then released, it no longer oscillates in a simple sinusoidal motion. Viscous effects appear to be much more dominant and change the frequency and amplitude of aileron motion. The motion appears to repeat every fourth oscillation, and an average oscillation frequency is about 35.3 Hz ($\kappa = 1.17$).

V. Concluding Remarks

For the most part, the agreement between numerical simulation and experimental data taken more than 30 years ago is quite good. Wind tunnel wall and three-dimensional effects could easily contribute to a greater difference in numerical simulation and experiment. The calculations carried on here were exploratory in nature, and clearly better numerical resolution should be provided in the vicinity of the moving shock wave. In any event, the numerical results demonstrate that such unsteady flow phenomenon as transonic aileron buzz can be successfully studied using computational procedures.

Appendix

When only central spatial-difference operators are used in Eq. (7), higher-order convection term accuracy can be easily obtained. This is accomplished by central differencing only the right-hand side operators, δ_ξ and δ_η, with the conventional five-point, fourth-order accurate-difference operators. For example, the model problem

$$\partial_t u + \partial_x u = 0 \qquad \text{(A1)}$$

can be differenced

$$(I + h\delta_x)(u^{n+1} - u^n) = -h\tilde{\delta}_x u^n + \beta(u^n - u^{n-1}) \qquad \text{(A2)}$$

where

$$\delta_x u_j = \frac{u_{j+1} - u_{j-1}}{2\Delta x} \qquad 0(\Delta x^2) \qquad \text{(A3)}$$

$$\tilde{\delta}_x u_j = \frac{-u_{j+2} + 8u_{j+1} - 8u_{j-1} + u_{j-2}}{12\Delta x} \qquad 0(\Delta x^4) \qquad \text{(A4)}$$

Because the second-order accurate spatial-difference operator works only on Δu, the accuracy of Eq. (A2) with $\beta = 1/3$ is consistent with a differencing that is second order in time and fourth order in space. The advantage of retaining the three-point spatial operator for the left-hand side of the equation is that a pentadiagonal inversion is avoided. With Euler implicit time differencing ($\beta = 0$, $h = \Delta t$), the scheme given by Eq. (A1) is unconditionally stable. However, unpublished analysis by Warming[15] shows that the scheme cannot be unconditionally stable when $\beta = 1/3$ and $h = 2\Delta t/3$. Nevertheless, in a limited number of calculations using this differencing in Eq. (7), no stability bound was found other than the nonlinear or variable coefficient bound that the basic scheme exhibits. If trapezoidal time differencing is used in Eq. (A2), the scheme is unstable for all values of Δt. Finally, we remark that when fourth-order accurate differencing is used, the metrics, Eq. (4), should be obtained with the same difference operator as in Eq. (A4) (see Ref. 1, Sec. IV, for background discussion).

References

[1] Steger, J. L., "Implicit Finite-Difference Simulation of Flow about Arbitrary Two-Dimensional Geometries," *AIAA Journal*, Vol. 16, July 1978, pp. 679-686.

[2] Brown, H. H., Rathert, Jr., G. A., and Clousing, L. A., "Flight-Test Measurements of Aileron Control Surface Behavior at Supercritical Mach Numbers," NACA RM A7A15, April 1947.

[3] Erickson, A. L. and Stephenson, J. D., "A Suggested Method of Analyzing for Transonic Flutter of Control Surfaces Based on Available Experimental Evidence," NACA RM A7F30, Dec. 1947.

[4] Landahl, M. T., *Unsteady Transonic Flow*, Pergamon Press, New York, 1961.

[5] Baldwin, B. S. and Lomax, H., "Thin Layer Approximation and Algebraic Model for Separated Turbulent Flows," AIAA Paper 78-257, 1978.

[6] Viviand, H., "Conservative Forms of Gas Dynamic Equations," *La Recherche Aerospatiale*, No. 1, Jan.-Feb. 1974, pp. 65-68.

[7] Beam, R. M. and Warming, R. F., "An Implicit Factored Scheme for the Compressible Navier-Stokes Equations," AIAA Paper 77-645, June 1977.

[8] Warming, R. F. and Beam, R. M., "On the Construction and Application of Implicit Factored Schemes for Conservation Laws," Symposium on Computational Fluid Dynamics, New York, April 16-17, 1977; *SIAM-AMS Proceedings*, Vol. 11, 1978, pp. 85-129.

[9] Desideri, J. A., Steger, J. L., and Tannehill, J. C., "On Improving the Iterative Convergence Properties of an Implicit Approximate-Factorization Finite Difference Algorithm," NASA TM-78495, June 1978.

[10] Thompson, J. F., Thames, F. C., and Mastin, C. M., "Automatic Numerical Generation of Body-Fitted Curvilinear Coordinate System for Field Containing any Number of Arbitrary Two-Dimensional Bodies," *Journal of Computational Physics*, Vol. 15, July 1974, pp. 299-319.

[11] Sorenson, R. and Steger, J. L., "Simplified Clustering of Nonorthogonal Grids Generated by Elliptic Partial Differential Equations," NASA TM-73,252, 1977.

[12] Tijdeman, H., "On the Motion of Shock Waves on an Airfoil with Oscillating Flap," *Symposium Transonicum II*, Springer-Verlag, 1975, pp. 49-56.

[13] Ballhaus, W. F. and Goorjian, P. M., "Implicit Finite Difference Computations of Unsteady Transonic Flows About Airfoils, Including the Treatment of Irregular Shock Wave Motions," AIAA Paper 77-205, 1977.

[14] Magnus, R. J., "Calculation of Some Unsteady Transonic Flows About the NACA 64A006 and 64A010 Airfoils," AFFDL Rept. TR-77-46, 1977.

[15] Warming, R. F., private communication, NASA Ames Research Center, Moffett Field, Calif., 1978.